HEALTH AND MEDICINE

An ultrasmall theranostic nanozyme for abdominal aortic aneurysm management and therapeutic efficacy monitoring

Wanling Liu[1,2], Yihong Zhang[1], Xiaomiao Cui[1], Qi Sun[1], Xiang Gu[1], Tong Li[1], Shicheng He[3], Zhexue Qin[2], Hui Wei[1,4,5,6]*

Abdominal aortic aneurysm (AAA) is a life-threatening condition lacking effective drug interventions, and its progression is difficult to predict, complicating early clinical management. Here, we present a reactive oxygen species–responsive theranostic nanozyme for AAA early intervention and efficacy monitoring, establishing a feedback loop between treatment and diagnostics. OZn, designed by encapsulating ultrasmall Prussian blue (SPBZn) within oxidation-sensitive dextran, targets aneurysm sites, where it responds to inflammatory microenvironments by releasing SPBZn. In vivo, SPBZn not only mitigated $CaCl_2$-induced aneurysm expansion and AAA progression in rat models but also enabled noninvasive diagnostic monitoring via urinalysis due to its enzymatic activities and renal metabolism. This theranostic nanozyme dynamically regulated therapeutic efficacy and provided feedback on disease progression. By preventing vascular rupture through early intervention and enabling precise drug administration, this work highlights a transformative strategy for integrating diagnostics and therapy to improve AAA management and clinical outcomes.

INTRODUCTION

Abdominal aortic aneurysm (AAA) is a life-threatening enlargement of the aorta and one of the leading causes of mortality and morbidity in the elderly (*1*, *2*). Guidelines recommend surgical intervention for large asymptomatic AAA, as well as symptomatic and ruptured cases (*3*, *4*). While surgical repair is the standard treatment for AAA, it is invasive, associated with complications, and has limited long-term effectiveness. Moreover, ~20 to 30% of patients undergoing endovascular repair require reintervention within 5 years, leading to reduced patient compliance and increased surgical risk and mortality (*5*–*7*). Patients with small asymptomatic aneurysms or those with anatomical constraints are often left untreated and placed under surveillance. However, AAA progression is nonlinear and unpredictable, with a high risk of sudden rupture, presenting substantial challenges for disease management (*8*). Despite being asymptomatic before rupture, AAA rupture is often lethal, with a mortality rate of 85 to 90% (*5*, *9*). Meanwhile, patients who usually undergo "clinical monitoring" face psychological stress and leave the risk of rupture unaddressed. These challenges highlight an urgent need for pharmacological therapies to slow aneurysm growth and reduce rupture risk. Unfortunately, there are no effective drugs to prevent aneurysm growth or delay rupture in clinical (*7*, *10*). Developing effective pharmacological treatment will provide safer, less invasive alternatives to surgery and offer a crucial approach for noninvasive therapeutic efficacy monitoring, addressing critical gaps in AAA management.

The pathogenesis of AAA is tangled and involves inflammatory cell infiltration, aortic wall dilatation and calcification, oxidative damage, and degradation of the arterial elastic matrix. Among these factors, oxidative stress and excessive reactive oxygen species (ROS) are the critical causes in driving early AAA progression (*8*, *11*–*18*), making ROS regulation a promising therapeutic target. ROS downregulation is crucial for mitigating inflammation, protecting vascular smooth muscle cells (VSMCs) from apoptosis, preserving extracellular matrix integrity, and inhibiting AAA progression. The redox balance in normal cells is maintained by antioxidant enzymes like superoxide dismutase (SOD) and catalase (CAT). Administering these antioxidant enzymes as a therapeutic intervention has shown potential in preventing AAA progression (*19*, *20*). However, the therapeutic use of natural enzymes is limited by their low stability and immunogenicity, necessitating the exploration of enzyme mimics for AAA management.

To address these challenges, we chose nanozymes, with enzyme-like theranostic capacities (*21*–*27*), for early intervention of AAA as well as noninvasive monitoring of therapeutic efficacy. We focused on Prussian blue (PB) nanozymes for their broad antioxidant mimetic activities, excellent biocompatibility, and tunable particle size. As shown in Fig. 1, we designed a ROS-triggerable nanozyme with targeted delivery to aneurysms by taking advantage of aneurysms' characteristic pathophysiology. Specifically, ultrasmall Prussian blue analog (SPBZn) was encapsulated within an oxidation-sensitive polymer, forming a theranositic agent, named OZn. OZn passively accumulated at aneurysm sites, releasing SPBZn in response to the inflammatory microenvironment, where its antioxidant activities efficiently prevented AAA progression. Moreover, ultrasmall SPBZn was metabolized by the kidneys, allowing for noninvasive diagnostic monitoring via urinalysis. This theranostic nanozyme not only facilitated early intervention and therapeutic efficacy assessment during treatment but also provided dynamic regulation and real-time

[1]Department of Biomedical Engineering, College of Engineering and Applied Sciences, Nanjing National Laboratory of Microstructures, Jiangsu Key Laboratory of Artificial Functional Materials, Nanjing University, Nanjing, Jiangsu 210023, P. R. China. [2]Department of Cardiology, Xinqiao Hospital, Army Medical University (Third Military Medical University), Chongqing 400037, P. R. China. [3]Jinfeng Laboratory, Chongqing 401329, P. R. China. [4]State Key Laboratory of Analytical Chemistry for Life Science, School of Chemistry and Chemical Engineering, Chemistry and Biomedicine Innovation Centre (ChemBIC), ChemBioMed Interdisciplinary Research Centre at Nanjing University, Nanjing University, Nanjing, Jiangsu 210023, P. R. China. [5]Nanozyme Laboratory in Zhongyuan, Henan Academy of Innovations in Medical Science, Zhengzhou, Henan 451163, P. R. China. [6]NMPA Key Laboratory for Biomedical Optics, Hangzhou, Zhejiang 310018, P. R. China.
*Corresponding author. Email: weihui@nju.edu.cn

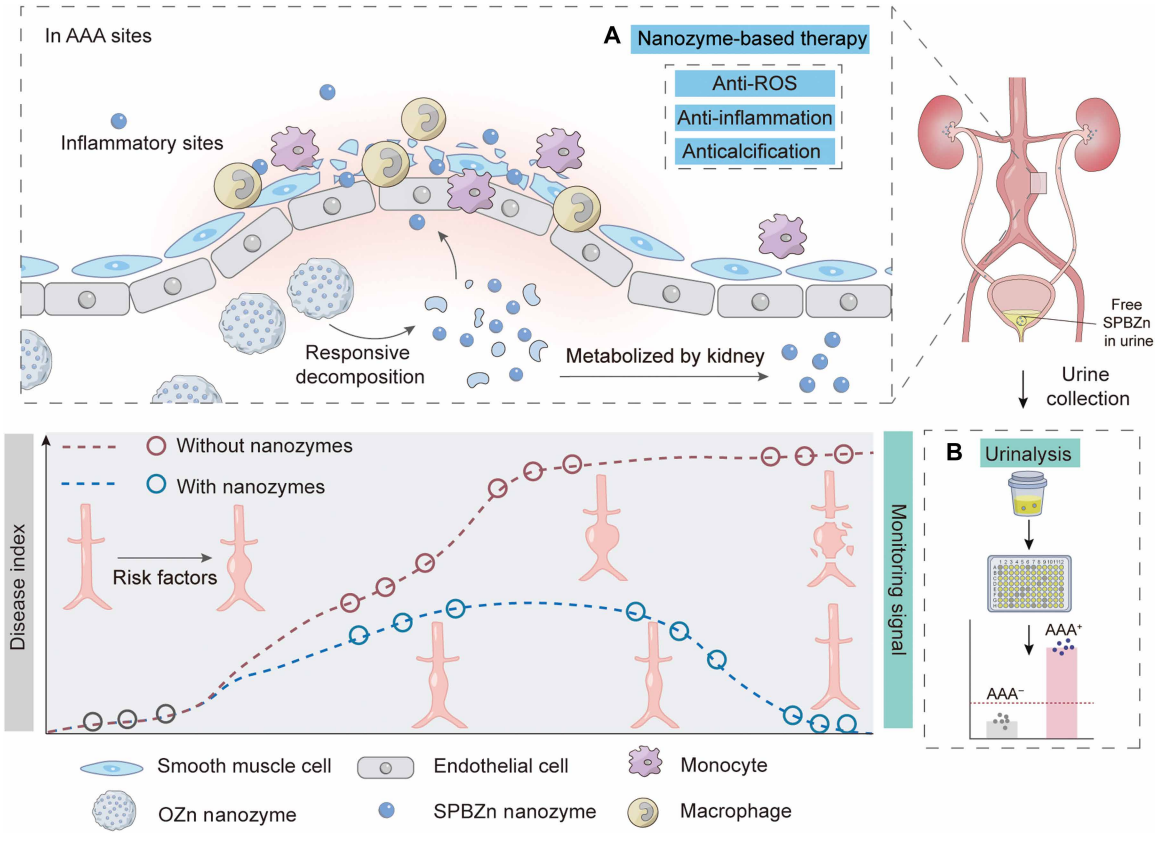

Fig. 1. Schematic illustration of OZn theranostic nanozyme for AAA management and therapeutic efficacy monitoring. (**A**) In vivo, OZn passively accumulated at aneurysm sites, releasing SPBZn in response to inflammation to prevent AAA progression via antioxidant activity. (**B**) In addition, the kidneys metabolized SPBZn, allowing noninvasive diagnostic monitoring via urinalysis based on its enzyme-mimicking activities. The monitoring signal can reflect the disease index. This theranostic approach integrates therapy and diagnostics, offering dynamic regulation and feedback for nanozyme therapeutic efficacy monitoring and effective AAA management.

feedback on disease status. This study highlights a synergistic integration of therapeutic and diagnostic functionalities, offering a promising approach for managing AAA.

RESULTS

Design, synthesis, and characterizations of ROS-responsive nanozyme

To engineer a ROS-responsive nanozyme, we first prepared the PB with ultrasmall size. We used an ethanol/water mixture as the solvent and polyvinylpyrrolidone (PVP) as the surface capping agent to get the ultrasmall PB (SPB) nanozyme (*28*). By doping PB with zinc ion, we obtained SPBZn nanozyme (*29*). The structures of SPB and SPBZn nanozymes were determined by powder x-ray diffraction (XRD) (Fig. 2A). The peaks at 17.5°, 24.6°, 35.2°, and 39.5° can be respectively assigned to the planes of PB. The result of XRD confirmed that the crystal structure of SPB and SPBZn was identical to that in the Joint Committee on Powder Diffraction Standards (JCPDS) card no. 33-1061. Transmission electron microscopy (TEM) imaging revealed that both the SPB and SPBZn nanozymes display a uniform size of about 3 nm (Fig. 2B). X-ray photoelectron spectroscopy (XPS) was used to analyze the effect of doping on the chemical states of these two ultrasmall nanozymes. The apparent peaks lying around 1021 eV indicated the presence of Zn in SPBZn (fig. S1E). To quantify the doping level, an inductively coupled plasma optical emission spectrometer (ICP-OES) gave an Fe:Zn ratio of 7.74:1 in SPBZn, indicating successfully Zn incorporation (table S1). Energy-dispersive x-ray spectroscopy and elemental mapping further revealed the presence and even distribution of Zn (fig. S2), which demonstrate successful Zn incorporation and homogeneous distribution within SPBZn. Collectively, these results confirm the successful synthesis of ultrasmall SPB and SPBZn nanozymes.

Next, we examined the antioxidant properties of both SPB and SPBZn. Enzymes play a crucial role in enzyme catalyzed therapy by facilitating anti-ROS cascade reactions. This process begins with the conversion of $O_2^{\bullet-}$ into H_2O_2 by SOD, followed by the transformation of H_2O_2 into water and O_2 by CAT. First, we assessed the SOD-like activity by monitoring the $O_2^{\bullet-}$ scavenging (Fig. 2C). Meanwhile, we measured the CAT-like activity using the dopamine-based CAT assay (*30*), confirming the higher CAT-like activity of SPBZn than SPB (Fig. 2D). With the superior SOD- and CAT-like activity, the SPBZn nanozyme exhibited superior antioxidant activity compared to SPB. Its excellent antioxidant activity indicated that the SPBZn nanozyme shows greater potential for AAA therapy.

Once the antioxidant activity of SPBZn nanozyme was confirmed, we used the oxidizable dextran (Oxi-DEX) carrier as the ROS-responsive element to achieve targeting. Oxi-DEX, composed of polysaccharide dextran (DEX), was chosen for its biocompatibility, biodegradability, and ease of modification (Fig. 2E). Pinacol

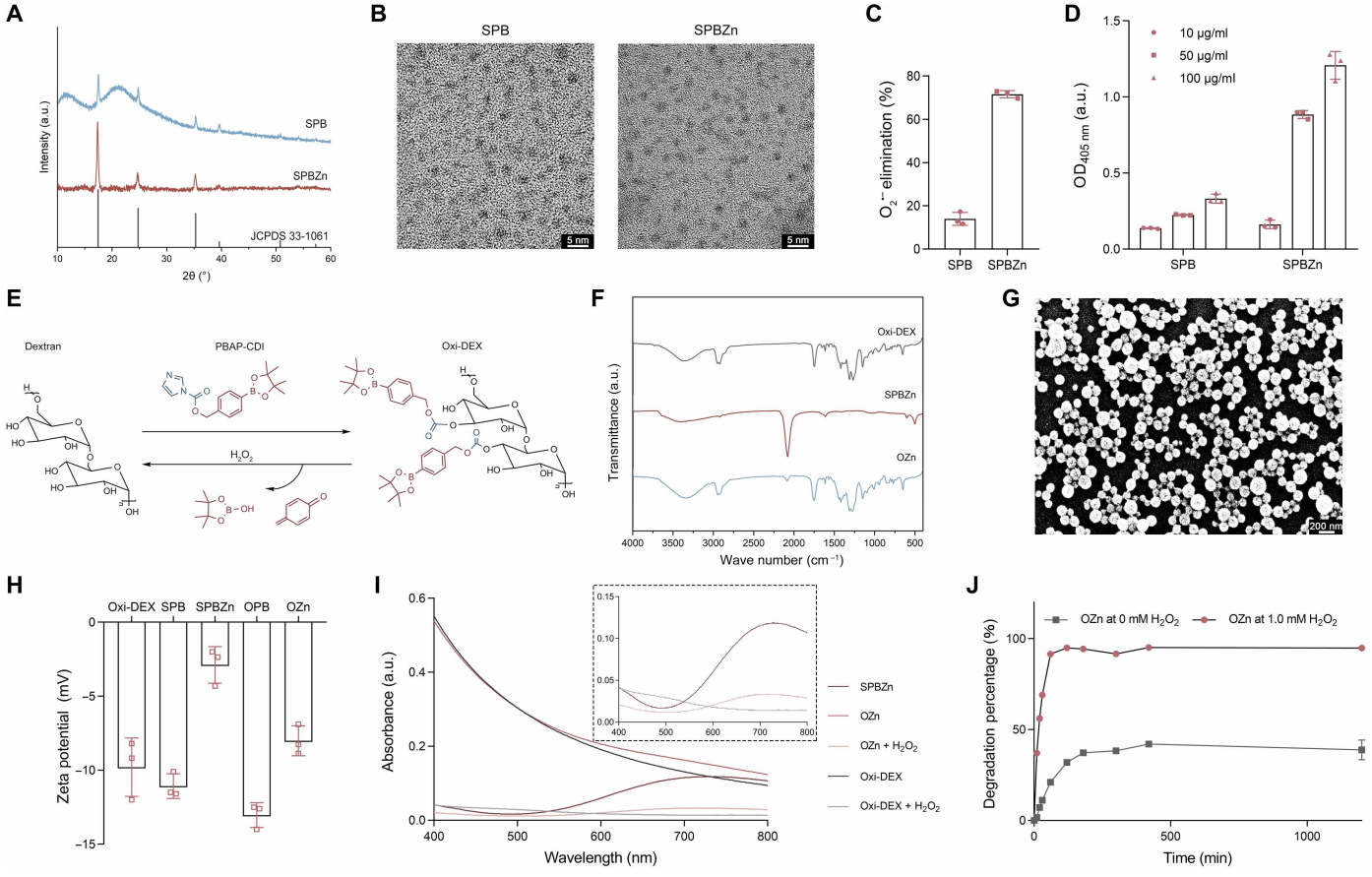

Fig. 2. Design, synthesis, and characterizations of ROS-responsive nanozyme. (**A**) XRD patterns of SPB and SPBZn. (**B**) TEM images of SPB and SPBZn. Scale bars, 5 nm. SOD- (**C**) and CAT-like (**D**) activities of SPB and SPBZn. Data are presented as mean ± SD ($n = 3$). (**E**) Schematic illustration of synthesis and degradation of Oxi-DEX. (**F**) Fourier transform infrared (FTIR) spectra of Oxi-DEX, SPBZn, and OZn. (**G**) SEM image of OZn. Scale bar, 200 nm. (**H**) Zeta potentials of Oxi-DEX, SPB, SPBZn, Oxi-DEX@SPB (OPB), and OZn. (**I**) In vitro release profiles of OZn in the presence of 1.0 mM H_2O_2. Inset: the spectra of SPBZn, OZn, and OZn + H_2O_2. (**J**) Degradation of OZn. Data are mean ± SD ($n = 3$). a.u., arbitrary units.

boronic esters, a type of arylboronic esters, were selected as triggering groups due to their convenient degradation mediated by H_2O_2 under physiological conditions (*31*). In addition, ROS-triggered oxidation of Oxi-DEX generates phenylboronic acid, which can adhere to cells or extracellular matrix at inflamed sites (*32*). These combined effects likely contribute to the targeting efficiency of the nanozyme. First, we synthesized the imidazoyl carbamate (fig. S4) and used it to modify DEX at the hydroxyl groups, forming Oxi-DEX. Then, SPBZn nanozyme was encapsulated in Oxi-DEX particles using standard emulsion techniques to form the ROS-responsive nanozyme, OZn. The incorporation of SPBZn was confirmed by Fourier transform infrared (FTIR) spectra, which shows that the OZn retained the characteristic peak of SPBZn representing C≡N stretching vibrations around 2070 cm^{-1} (*29*). Moreover, SPBZn showed negligible impact on the structure of Oxi-DEX (Fig. 2F). A scanning electron microscope (SEM) and dynamic light scattering (DLS) indicated that the OZn nanozyme was nearly spherical (Fig. 2G), with a mean diameter of 120 ± 15 nm (figs. S6 and S7). In addition, all nanozymes exhibited negative zeta potential values (Fig. 2H), which can target the inflammation lesion site effectively. The OZn retained the SOD- and CAT-like activities (fig. S8).

Next, we examined the H_2O_2-mediated degradation behaviors of OZn nanozyme. After incubating OZn with H_2O_2, one of the most common ROS, the ROS-responsive degradation profiles were recorded by an ultraviolet-visible (UV-vis) spectrophotometer (Fig. 2I). The UV-vis absorption spectra of SPBZn after incubation with H_2O_2 are shown in the inset of Fig. 2I. Degradation analysis revealed that less than 50% of the total SPBZn was released from OZn after 72 hours in phosphate-buffered saline (PBS) (Fig. 2J). In contrast, the release of SPBZn from OZn was substantially accelerated by H_2O_2. Nearly complete release of SPBZn was observed after 1 hour, demonstrating a marked increase compared to conditions without H_2O_2. These in vitro experiments confirmed the ROS-responsive release properties of the OZn nanozyme. Before testing cellular bioactivity, we confirmed electron spin resonance (EPR) that SPBZn does not catalyze $^{\bullet}OH$ formation from H_2O_2 via Fenton reaction, ensuring that its ROS scavenging activity is not compromised (fig. S9).

In vitro cellular bioactivity of nanozyme

The primary pathological characteristics of AAA involve changes in the extracellular matrix, which lead to the degeneration and loss of VSMCs and the accumulation and activation of inflammatory cells

(*7*, *17*, *18*). VSMCs play a pivotal role in AAA progression, and their impaired function and eventual loss are central to the process. In addition, given the substantial and unique contributions of monocytes and macrophages in the initiation and early progression of AAA (*11*), we also took these cells into account. We assessed the cellular uptake profiles of OZn in different cells first. To this end, a fluorescent conjugate, fluorescein isothiocyanate (FITC)–labeled OZn (FITC-OZn), was synthesized (fig. S10). Flow cytometric analysis showed that the uptake of FITC-OZn increased in a concentration-dependent manner in VSMCs, macrophages, and monocytes (fig. S11). Both OZn and SPBZn showed no cytotoxicity in the primary vascular cells (fig. S12).

Calcification, characterized by the deposition of calcium phosphate crystals in the medial layer of blood vessel walls, poses a notable risk for AAA rupture (*16*, *33*). VSMCs play a crucial role in the process of vascular calcification (*15*, *34*). We investigated whether nanozymes could protect VSMCs from calcification induced by calcium and inorganic phosphorus (Ca/Pi) (Fig. 3A). Following exposure to Ca/Pi, Alizarin Red staining revealed pronounced calcium buildup in the model group (Fig. 3D). Treatment with the OZn nanozyme resulted in a notable reduction in relative calcium deposition compared to treatments with Oxi-DEX and OPB (Fig. 3G).

Oxidative stress is widely recognized as a contributing factor in the development of aortic aneurysms and is linked to the regulation of VSMC function. Both VSMCs and infiltrating inflammatory cells are capable of contributing to the elevation of ROS levels within the vessel wall (*2*, *11*, *14*). Cells were treated with H_2O_2 to simulate the overproduction of intracellular ROS, where cells cultured with medium alone served as the normal control. To directly observe intracellular responsiveness and subcellular localization, we performed fluorescence microscopy. In the presence of H_2O_2, the FITC-OZn signal increased, consistent with ROS-mediated shell cleavage (figs. S13 and S14). The ability of OZn to scavenge intracellular ROS was monitored with a fluorescent probe for intracellular ROS, 2′,7′-dichlorofluorescein diacetate (DCFH-DA) (Fig. 3B). Fluorescence microscopy imaging confirmed that the OZn-treated group exhibited lower DCFH-DA fluorescence intensity in VSMCs compared to the Oxi-DEX and OPB groups (Fig. 3, E and H). Similar effects of OZn were observed in the monocytes (fig. S15) and macrophages (fig. S16). In addition, superoxide production was detected using dihydroethidium (DHE) staining (fig. S17). The lowest level of red fluorescence in the OZn group revealed that OZn significantly reduced the levels of $O_2^{\bullet-}$ in VSMCs.

Crucially, ROS also triggers apoptosis of VSMCs (*35*, *36*). Mechanistically, the reduction of VSMCs in the medial layer through apoptosis contributes to the progression of AAA (*2*, *35*, *37*). Treatment with H_2O_2 resulted in substantial VSMC apoptosis. However, preincubation with the OZn nanozyme mitigated H_2O_2-induced VSMC apoptosis (Fig. 3F). Among the indicated treatments, OZn demonstrated the most pronounced beneficial effects (Fig. 3I). Consequently, OZn effectively inhibits H_2O_2-induced VSMC apoptosis by reducing intracellular ROS generation. To this end, OZn

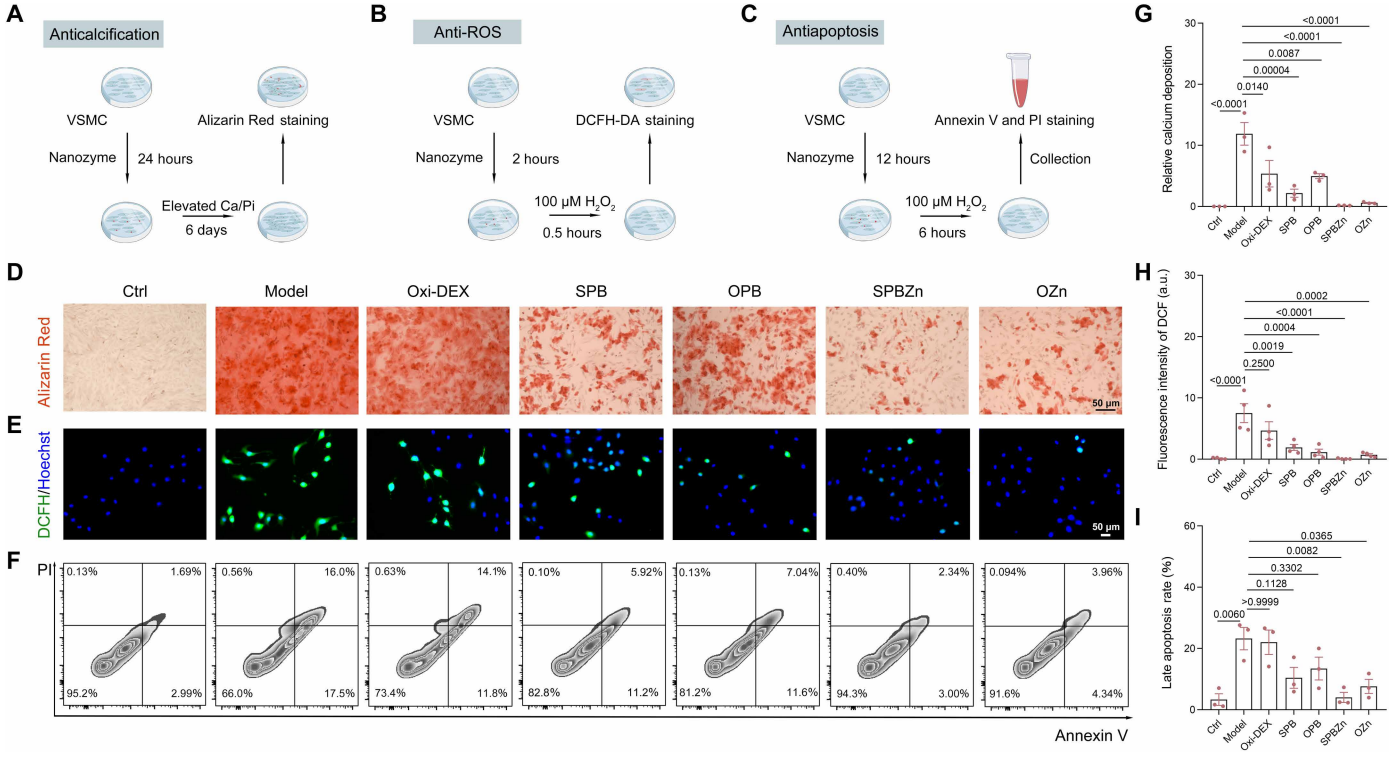

Fig. 3. In vitro activities of nanozymes in VSMCs. (**A**) Experimental protocol: in vitro anticalcification effects of different nanozymes. (**B**) Schematic illustration of the nanozymes' capacity to scavenge ROS. (**C**) Schematic illustration of the antiapoptotic capacity of nanozymes in vitro. (**D**) Representative microscopic images of VSMCs stained with Alizarin Red. Scale bar, 50 μm. (**E**) Fluorescence microscopy images of VSMC staining with DCFH. Scale bar, 50 μm. (**F**) Flow cytometric profile apoptotic VSMCs after induction with H_2O_2. Quantitative analysis of (**G**) the relative calcification ($n = 3$), (**H**) the average optical density of DCF ($n = 4$), and (**I**) the late apoptosis rate of VSMCs ($n = 3$). Data are mean ± SD and analyzed by one-way analysis of variance (ANOVA) and Student's *t* test.

scavenged ROS in cells and reduced apoptosis and calcification in VSMCs, which should have great promise in AAA prevention.

In vivo targeting capability of OZn nanozyme

Next, we verified the in vivo targeting capability of nanozyme. A typical $CaCl_2$-induced AAA model in rats was established for the in vivo targeting study. FITC-OZn was used to verify the targeting ability of ROS-responsive OZn nanozyme to aneurysmal aortas (Fig. 4A). Fluorescent signals were observed at the injury site of the abdominal aortas isolated from AAA^+ rats 8 hours after intravenous injection (Fig. 4B). Ex vivo imaging revealed significantly higher fluorescent signals in the aneurysmal aortas isolated from AAA^+ rats compared to AAA^- rats (Fig. 4E). Fluorescence imaging on cryosections confirmed the accumulation of OZn in aneurysmal aortas, with immunofluorescence staining revealing the localization of FITC fluorescence in $F4/80^+$ macrophages (Fig. 4C) and α-SMA^+ VSMCs (Fig. 4D) within the abdominal aorta cryosections. In addition, high OZn-VSMC and OZn-macrophage colocalization was observed (fig. S18). These results demonstrated that the intravenously administered OZn nanozyme could effectively target aneurysmal aortas. Notably, OZn accumulated in aneurysmal lesions is primarily internalized by inflammatory cells and VSMCs, underscoring its capacity to simultaneously affect the primary cell types involved in the pathology of AAA. In a separate study, we found that FITC-OZn accumulated in the aneurysmal lesion and was sustained for at least 24 hours (Fig. 4F and fig. S19). These results collectively demonstrate that the OZn nanozyme efficiently targets aneurysms and remains localized at the lesion site for an extended period.

Diagnosis of AAA by urinalysis

Leveraging the targeting and ROS-responsive release capabilities of OZn, we aimed to demonstrate its diagnostic potential for AAA through urinalysis (Fig. 5A). First, the kidney metabolism and urinary excretion of OZn following intravenous administration were investigated. The SPBZn nanozyme released from OZn, with an ultrasmall size (<5 nm), can be metabolized by the kidneys and excreted in the urine (*23*). To evaluate the metabolism and excretion of OZn nanozyme, FITC-OZn was administered. The urine samples were collected, and fluorescence images were obtained using the in vivo imaging system (IVIS) spectrum imaging following intravenous

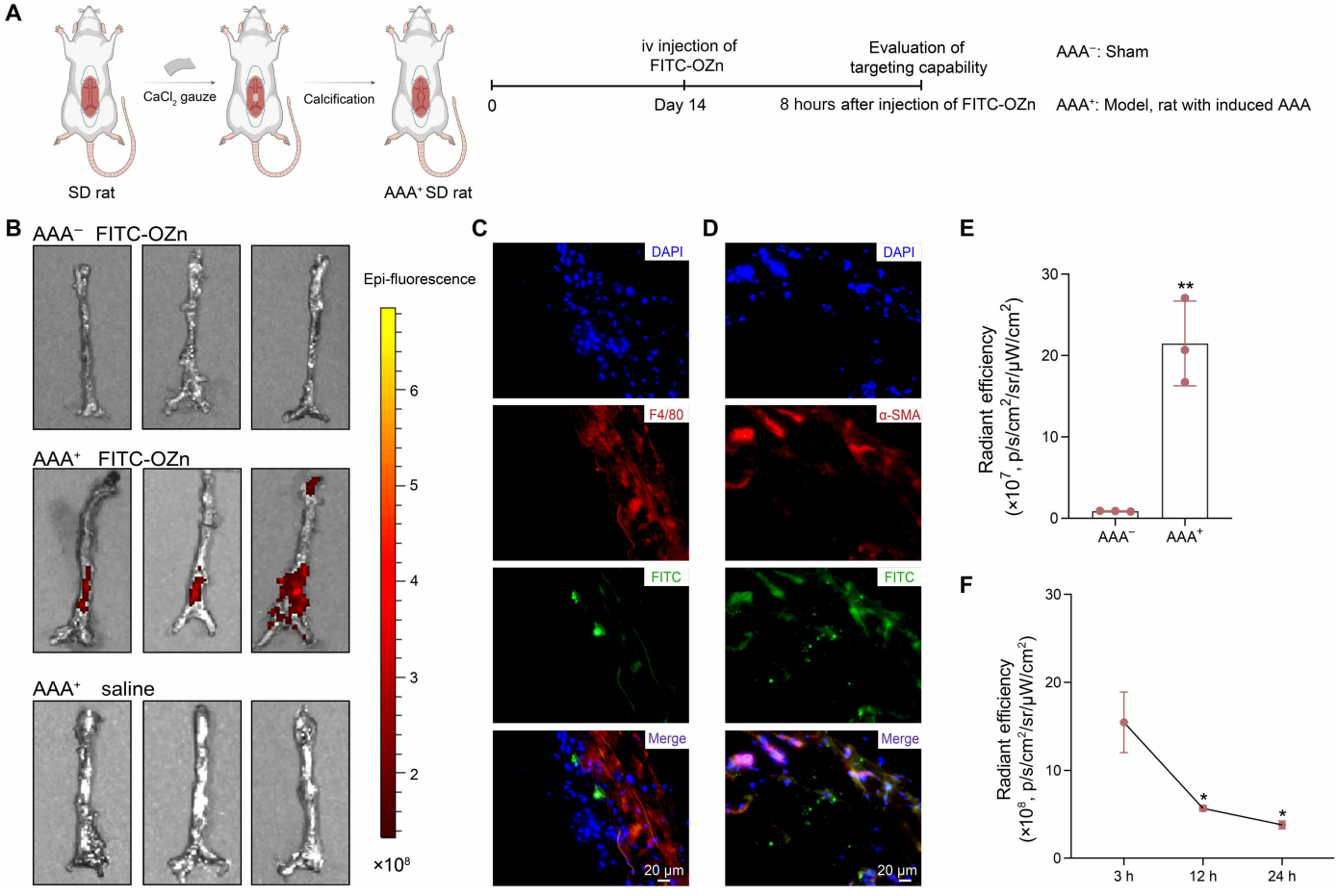

Fig. 4. In vivo targeting of OZn in AAA rats by intravenous delivery. (**A**) Schematic illustration of $CaCl_2$-induced AAA in rats and the schedule for in vivo targeting investigations. (**B**) Fluorescence images of aneurysmal aortic tissue distribution profiles of FITC-OZn after intravenous (iv) injection. Immunofluorescence analysis of the distribution of FITC-OZn in cryosections of aneurysmal aortic tissues and colocalization of FITC-OZn with (**C**) $F4/80^+$ macrophages and (**D**) α-SMA^+ VSMCs in aneurysms. Scale bars, 20 μm. (**E**) Quantitative analysis of FITC-OZn in aneurysmal aortic of AAA^+ and AAA^- rats. Data are mean ± SD ($n = 3$). (**F**) Quantitative intensities of FITC-OZn in the aneurysmal aortic of AAA^+ rats with times at 3, 12, and 24 hours after injected intravenously. Data are mean ± SD ($n = 3$). Statistical differences were analyzed by one-way ANOVA and Student's *t* test: $^*P < 0.05$ and $^{**}P < 0.01$. SD, Sprague-Dawley; DAPI, 4′,6-diamidino-2-phenylindole; h, hours.

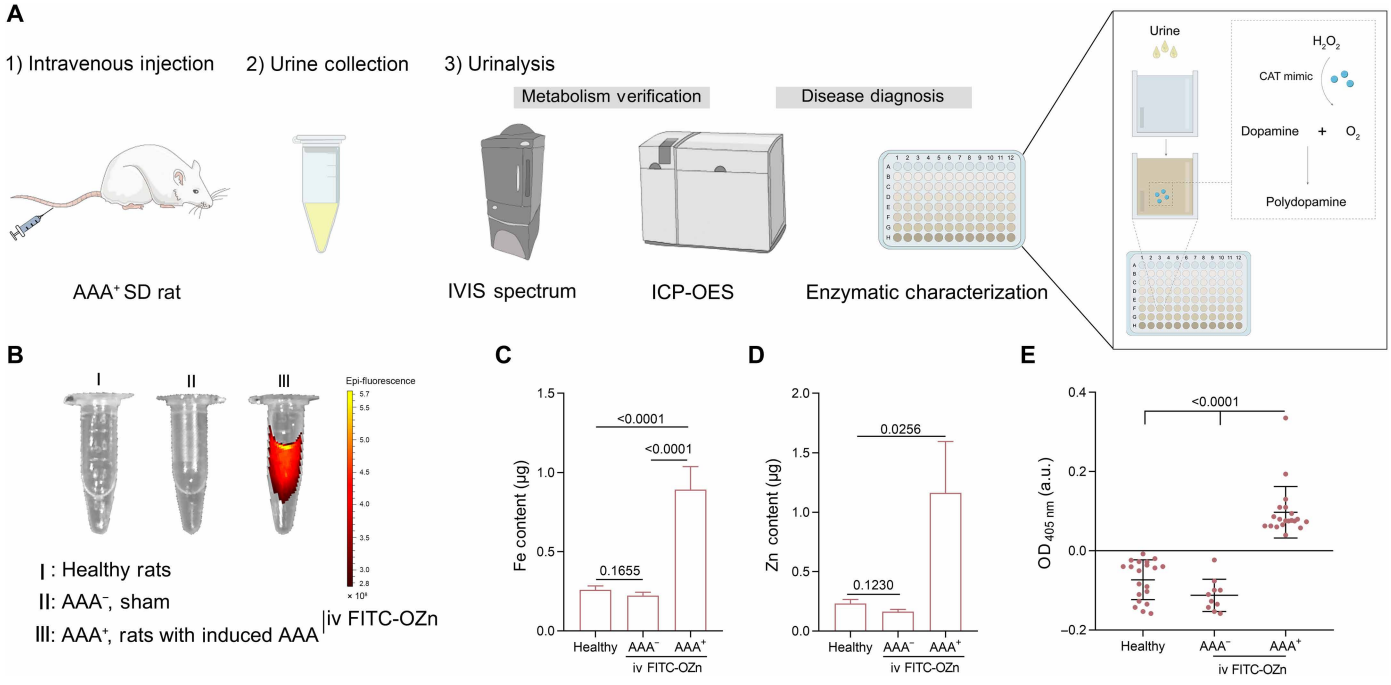

Fig. 5. Diagnosis of AAA by urinalysis. (**A**) Schematic illustration of urinalysis. FITC-OZn nanozymes were intravenously injected into AAA^+ rats, and urine was collected. Urine was analyzed using a CAT-like activity assay and ICP-OES to measure the Fe and Zn content. (**B**) Representative fluorescence images of urine. The content of (**C**) Fe and (**D**) Zn in the urine was assessed by ICP-OES ($n = 10$). Statistical analysis to compare median values between groups was determined by the Mann-Whitney *U* test. (**E**) CAT-like activities of urine. Data are mean ± SD and analyzed by one-way ANOVA and Student's *t* test.

injection of FITC-OZn. Notably, high fluorescence was observed exclusively in the urine of the AAA^+ group (Fig. 5B). Since the size of OZn is about 150 to 200 nm, it cannot be directly excreted by kidneys. However, in the high ROS environment of AAA, FITC-DEX was released via FITC-OZn degradation. The DEX with M_w (weight-average molecular weight) = 10 kDa can be rapidly metabolized by the kidneys (*38*, *39*). The results showed that fluorescence, primarily from FITC-DEX, accumulated in the kidneys of AAA^+ rats (fig. S20). These fluorescence imaging results confirmed both the targeting and ROS-responsive capabilities of the OZn nanozyme as well as its renal excretion.

To further confirm the urinary excretion of SPBZn, we used ICP-OES to measure the content of Fe and Zn in the urine. As shown in Fig. 5 (C and D), there was a significant difference in the content of Fe and Zn between the normal and AAA^+ rats. These results demonstrated that SPBZn was specifically released from OZn in AAA^+ rats after oxidative responsive decomposition. Eventually, the SPBZn excreted in the urine, likely due to the elevated ROS levels characteristic of the disease.

Owing to its excellent CAT-like activity, SPBZn exhibits a distinct CAT-like catalytic signal in the urine of AAA rats. To noninvasively monitor AAA, we measured the catalytic signal of SPBZn in urine using dopamine-enabled universal assay. Only the AAA^+ group exhibited a relatively high level of OD_{405} (optical density at 405 nm), reflecting the CAT-like activity in the urine (Fig. 5E). Whereas the AAA^- group exhibited a negative signal even when administered with OZn at the same dose. The healthy rats' urine also showed a negative CAT-like activity signal. In addition, the ICP-OES results were consistent with the CAT-like activity detection, which confirmed the catalytic signal from SPBZn. These results demonstrated that SPBZn is specifically released from OZn in AAA rats and eventually excreted in the urine, likely due to the elevated ROS levels characteristic of the disease. This established a noninvasive diagnostic method for AAA via urinalysis.

In vivo therapeutic efficacy of ROS-responsive nanozyme in AAA rats

On the basis of the promising results mentioned above, we evaluated the therapeutic efficacy of the ROS-responsive nanozyme OZn in AAA rats. On day 2 after $CaCl_2$-induced injury, saline was injected intravenously into the model group, while different nanozymes and Oxi-DEX were administered to other groups twice a week for 3 weeks (Fig. 6A). At the same dose of 5 mg/kg, OZn exhibited the most pronounced therapeutic effect, as demonstrated by histological examination, showing a relatively intact vascular structure (Fig. 6B-i and fig. S21). Alizarin Red staining showed the largest calcium deposition in the model group. Although SPBZn showed considerable effectiveness, OZn achieved the most pronounced effect (Fig. 6, B-ii and E). Verhoeff-Van Gieson (EVG) staining revealed severe damage to abdominal aortas and elastin degradation in the model group, whereas these pathological abnormalities were alleviated by OZn treatment (Fig. 6, B-iii and F). Immunofluorescence staining of the α-SMA showed significant VSMC apoptosis, especially in the AAA model group, but OZn significantly attenuated this condition (Fig. 6C). Correspondingly, the terminal deoxynucleotidyl transferase–mediated deoxyuridine triphosphate nick end labeling (TUNEL) assay indicated that the OZn nanozyme remarkably inhibited cell apoptosis in aneurysmal lesions (Fig. 6, I and J). These results demonstrated that

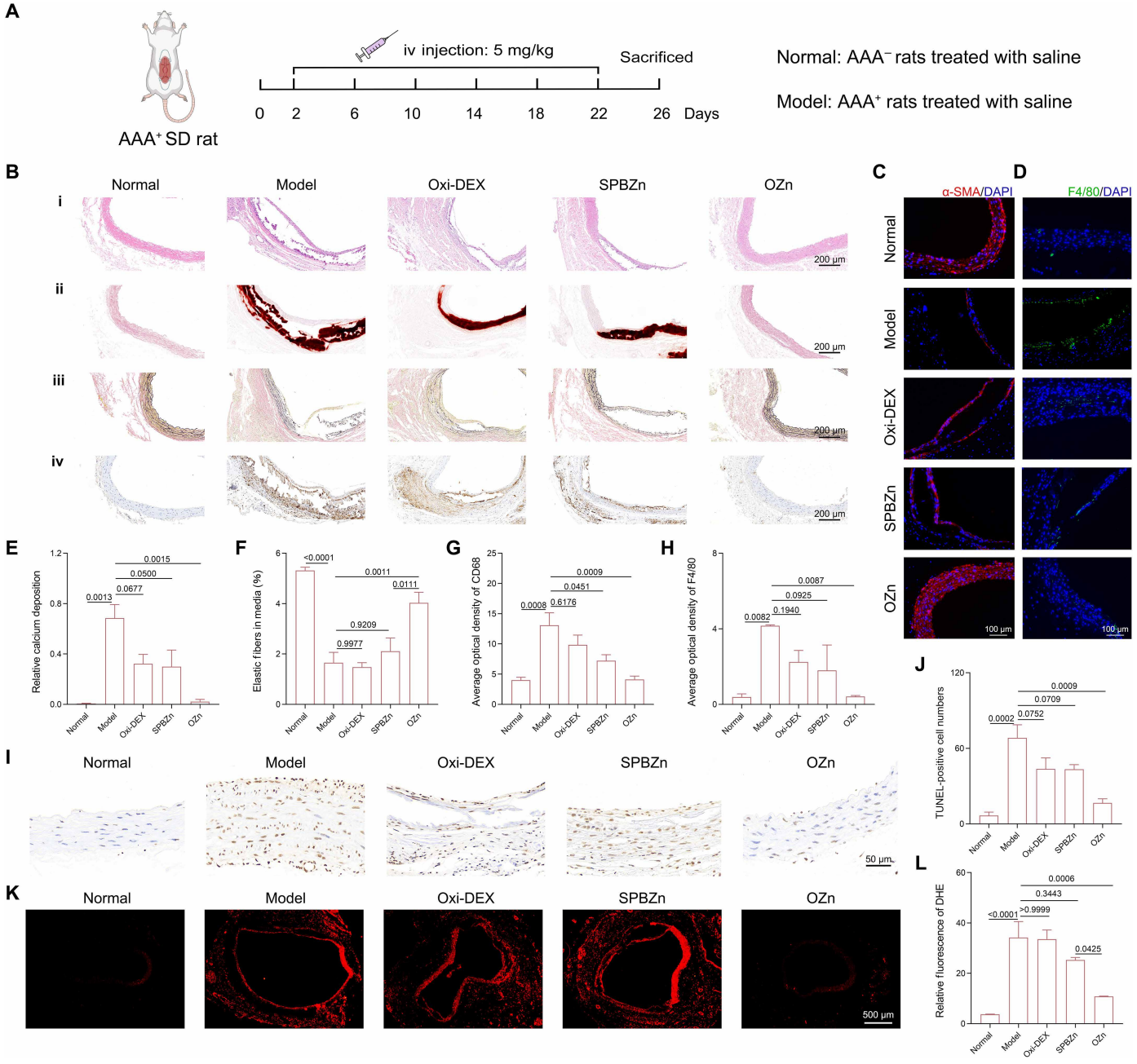

Fig. 6. In vivo therapeutic efficacy of different nanozymes in AAA rats. (**A**) Schematic illustration of $CaCl_2$-induced AAA in rats and the treatment protocols. (**B**) Representative images of aortas sections stained with (i) H&E, (ii) Alizarin Red, (iii) EVG, and (iv) an antibody against CD68. Scale bars, 200 μm. (**C** and **D**) Immunofluorescence staining of α-SMA and F4/80, respectively. Scale bars, 100 μm. Quantitative analysis of the relative calcium deposition in the abdominal aortas (**E**), the elastic fibers in media (**F**), and the average optical density of CD68 (**G**) and F4/80 (**H**). (**I**) Representative microscopy images of TUNEL-stained sections of aortic tissues from rats after indicated treatments. Scale bar, 50 μm. (**J**) Quantitative data of the number of apoptotic cells in aneurysmal lesions based on TUNEL staining. (**K**) Fluorescence images of DHE-stained cryosections of abdominal aortas from rats after indicated treatments. Scale bar, 500 μm. (**L**) Quantitative analysis of fluorescence intensities of DHE. Data are mean ± SD and analyzed by one-way ANOVA and Student's *t* test.

the OZn nanozyme more effectively prevented aneurysm expansion in AAA rat models compared to a nonresponsive control, by inhibiting VSMC apoptosis and elastin degradation.

To a large extent, AAA is an inflammation-related disease. Staining with CD68 (Fig. 6B-iv) and F4/80 (Fig. 6D), two representative markers of inflammatory macrophages, revealed that inflammatory cell infiltration and activation were attenuated following treatment with the OZn nanozyme (Fig. 6, G and H). DHE-stained sections of abdominal aortas in the model group exhibited high levels of red fluorescence. In contrast, the red fluorescence in the OZn nanozyme group was significantly lower than that in the other groups (Fig. 6, K and L). These results indicated that oxidative stress was significantly

mitigated by the intravenously delivered OZn nanozyme. Accordingly, these findings demonstrated that, by targeting aneurysms and releasing SPBZn in response to the inflammatory microenvironment, OZn effectively attenuated systemic oxidative stress, cell apoptosis, and inflammation in the abdominal aortas. These results confirmed that the OZn nanozyme exhibited superior therapeutic efficacy in preventing aneurysm expansion in AAA rats.

Therapeutic efficacy of OZn in a prolonged AAA model

The in vivo efficacy of OZn was further evaluated in AAA rats subjected to $CaCl_2$-induced injury over a prolonged period, which is more representative of clinical settings. Different nanozymes were administrated intravenously at a dose of 5 mg/kg on day 10 after $CaCl_2$ induction (Fig. 7A). In this study, clopidogrel, a medication commonly used for cardiovascular disease treatment, was included as a positive control. After four-time treatments, OZn demonstrated desirable efficacy by suppressing aortic expansion (Fig. 7B-i and fig. S22) and partially preventing elastin degradation to some degree by EVG staining (fig. S23). In addition, the immunofluorescence staining of the α-SMA showed that the OZn protected the structural integrity of VSMCs (Fig. 7C). Matrix remodeling, characterized by changes in the expression of matrix metalloproteinase 2 (MMP-2) and MMP-9, is associated with AAA progression (*7*). Immunohistochemistry analyses revealed that the levels of MMP-2 and MMP-9 were remarkably reduced by the OZn treatment (Fig. 7, B-iii and B-iv, F, and G). Alizarin Red staining showed a reduction in calcium deposition after OZn therapy (fig. S24). This result was further confirmed by ICP-OES, which measured the Ca content in the abdominal aortic. ICP-OES analysis indicated a significantly high Ca content in the model group, while OZn therapy reduced the Ca content to levels comparable to those in the normal group (Fig. 7I). The ICP-OES results were consistent with the Alizarin Red staining, confirming that OZn effectively reduces calcification. Furthermore, immunohistochemistry analysis of CD68 (Fig. 7B-ii), immunofluorescence staining of F4/80 (Fig. 7D), and DHE-stained fluorescence images of abdominal aortas (fig. S25) demonstrated that the OZn attenuated inflammatory cell infiltration and activation while also inhibiting aortic oxidative stress (Fig. 7, E and H). Moreover, the therapeutic efficacy of OZn was superior to that of clopidogrel (fig. S26), particularly in inhibiting inflammatory cell infiltration (Fig. 7E). With its ROS-responsive properties, OZn exhibited greater antianeurysmal activity than the SPBZn nanozyme alone. These results clearly substantiated that the OZn nanozyme can markedly prevent $CaCl_2$-induced AAA progression in rats, even after a long-term injury.

Therapeutic efficacy monitoring with urinalysis

Clinically, the postoperative recovery is followed by imaging. However, the imaging is not only expensive but also harmful to patients due to the use of contrast reagents. This clinical dilemma highlights the need to assess the therapeutic efficacy of nanozyme during treatment in a more facile way. Moreover, the establishment of interactive feedback between diagnosis and treatment progression would also minimize the drug dosage. Encouraged by the dual diagnostic and therapeutic functionality of OZn, we next investigated the correlation between urinalysis results and AAA disease progression. To evaluate this relationship, AAA rats were treated with OZn at different stages of disease progression, with two treatments per stage (Fig. 7J). In the pretherapy phase across all three stages, OD_{405} signals were negative. However, at the end of therapy in stages 1 and 2, OD_{405} levels remained positive (Fig. 7K and fig. S27, A and B). Correspondingly, pathological analysis revealed no significant therapeutic effect, as the aortic expansion persisted to some extent (fig. S28). These findings suggest that the therapy at stages 1 and 2 was insufficient and needed to be continued. In contrast, at the end of stage 3, urinalysis results turned negative, showing no significant difference from pretherapy levels but a significant difference compared to the beginning of therapy (fig. S27C). This indicates that treatment can be concluded at this stage. Notably, prolonged OZn therapy in stage 3 led to greater suppression of aortic expansion (Fig. 7L and fig. S28), highlighting the bidirectional feedback between therapeutic efficacy and urinalysis results.

Overall, OD_{405} levels consistently decreased as therapy advanced (Fig. 7K). Pathological analysis further confirmed that extended OZn therapy notable suppressed aortic expansion, demonstrating its therapeutic efficacy (Fig. 7L and fig. S28). The alignment of urinalysis results with therapeutic outcomes underscores the potential of this strategy to dynamically regulate diagnostic feedback and treatment efficacy. Unlike conventional approaches requiring separate diagnostic imaging and therapeutic interventions, this nanozyme directly modulates the pathological microenvironment while simultaneously generating SPBZn as a diagnostic signal. This "treatment while monitoring" strategy markedly enhances clinical efficiency and reduces the need for additional invasive tests.

Biosafety assessment

To assess the biosafety of OZn, the levels of typical hematological parameters following OZn injection were first determined. A complete blood count in rats indicated that the levels of red blood cells, white blood cells, platelets, and hemoglobin remained within normal ranges (fig. S29). Next, we evaluated the safety of the full treatment regimen. Histological examination of hematoxylin and eosin (H&E)–stained sections from major organs (heart, liver, spleen, lung, and kidney) showed no apparent toxicity in any experimental group (fig. S30). In addition, IVIS spectrum imaging demonstrated the biodistribution of OZn mainly in the liver and kidney (figs. S20 and S31). The OZn nanozyme was found to be metabolized within 24 hours (fig. S31). We further quantified the biodistribution of Fe and Zn, the main elements of OZn by ICP-OES. Signals were detectable across organs, indicating limited off-target accumulation and supporting the biosafety of the OZn nanozyme (fig. S32). Therefore, these results suggested that intravenous administration of the OZn nanozyme is safe at the examined dose, confirming its biosafety.

DISCUSSION

We have developed a transformative strategy for AAA management that integrates early intervention and efficacy monitoring, establishing a feedback loop between treatment and diagnostics. The versatile nanozyme presented in this work, with its diverse enzymatic activities and renal-clearable properties, facilitates noninvasive diagnostic monitoring through urinalysis while effectively inhibiting aneurysm expansion and mitigating AAA progression. This work highlights the versatility of nanozymes, demonstrating that their enzyme-like catalytic activity and multifunctionality can be precisely engineered to address diverse biomedical application needs. It also offers a remarkable advancement in the field of nanozyme-enabled theranostics. Furthermore, this approach presents an integrated strategy for AAA management with potential for clinical translation.

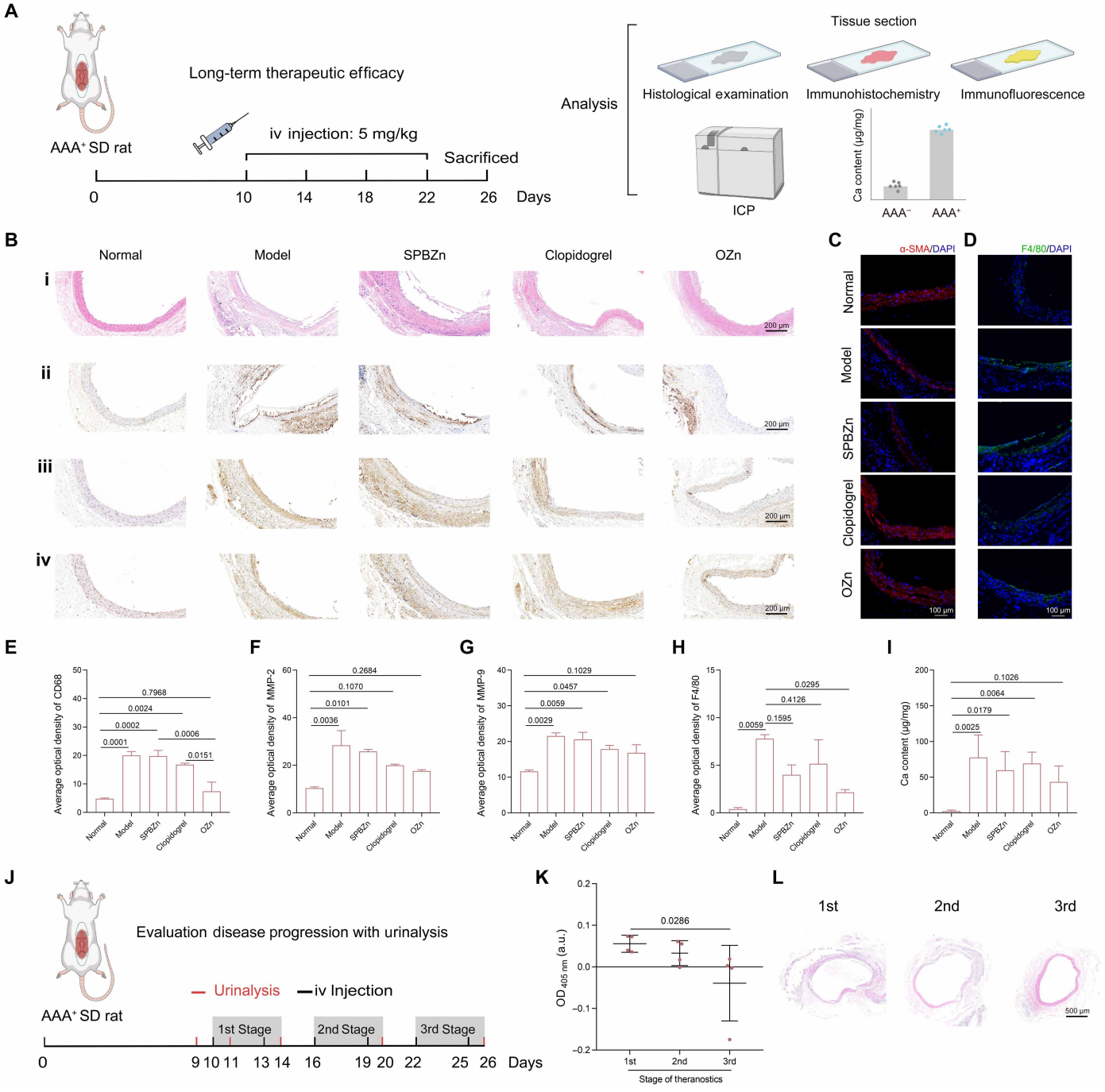

Fig. 7. In vivo therapeutic studies of OZn in AAA rats subjected to $CaCl_2$-induced abdominal aortic injury for a prolonged period. (**A**) Schematic illustration of the treatment protocols. (**B**) Histopathological sections of abdominal aortas stained with (i) H&E and immunohistochemistry analysis of (ii) CD68, (iii) MMP-2, and (iv) MMP-9 in aneurysmal aortas. Scale bars, 200 μm. (**C** and **D**) Immunofluorescence staining of the α-SMA and F4/80, respectively. Scale bars, 100 μm. (**E** to **H**) Quantitative analysis of the average optical density of (E) CD68, (F) MMP-2, (G) MMP-9, and (H) F4/80. (**I**) Ca content of AAAs, assessed by ICP-OES. Data are presented as mean ± SD ($n = 4$). (**J**) Schematic illustration of evaluation disease progression with urinalysis. (**K**) CAT-like activities of urine after treatment by OZn in every stage ($n = 4$). Data are mean ± SD and analyzed by one-way ANOVA and Student's *t* test. (**L**) Representative images of aortas sections stained with H&E. Scale bar, 500 μm.

MATERIALS AND METHODS

Chemicals and reagents

$K_3[Fe(CN)_6]$ (potassium ferricyanide), $K_4[Fe(CN)_6]\cdot 3H_2O$ (potassium ferrocyanide), $FeCl_3$ (ferric chloride), NaCl (sodium chloride), $C_6H_8O_7$ (anhydrous citric acid), $MgSO_4$ (magnesium sulphate), $CHCl_3$ (trichloromethane), and dry CH_2Cl_2 (dichloromethane) were purchased from Sinopharm Chemical Reagent Ltd. (Shanghai, China). $ZnCl_2$ (zinc chloride) was purchased from Macklin Biochemical Co. Ltd. (Shanghai, China). DEX (Mw = 10 kDa) was provided by XiYa Reagent Ltd. (Shandong, China). 4-Dimethylaminopyridine (DMAP), carbonyldiimidazole (CDI), and 4-hydroxyphenylboronic acid pinacol ester (PBAP) were purchased from Tianjin Xiensi Biochemical Technology Co. Ltd. (Tianjin, China). H_2O_2 (hydrogen peroxide, 30%), HCl (hydrochloric acid), C_2H_5OH (ethanol), CH_3OH (methanol), PVP (k30), polyvinyl alcohol (PVA; Mw, ~145,000), dibutyltin dilaurate, dry dimethyl sulfoxide (DMSO), FITC, and pyridine were purchased from Aladdin (Shanghai, China). $CaCl_2$ (calcium chloride) was purchased from Sigma-Aldrich (St. Louis, USA). SOD assay kits (WST-1), 5,5-dimethyl-1-pyrroline *N*-oxide (DMPO), and Cell Counting kit-8 (CCK-8) were purchased from Dojindo Laboratories (Kumamoto, Japan). Dopamine was purchased from Yuanye Bio-Technology Co. Ltd. (Shanghai, China). Hoechst, 4′,6-diamidino-2-phenylindole, DCFH-DA, and annexin V–FITC apoptosis detection kits were purchased from Beyotime Chemical Reagent Co. Ltd. (Shanghai, China). All chemical reagents were used as received without further purification. All aqueous solutions used in the experiments were prepared with deionized water (18.2 megohm·cm; Millipore).

Instrumentations

XRD data were recorded with 5°/min on a D8 advance x-ray diffractometer (Bruker-AXS, Germany). DLS and zeta potential results were recorded by a Zetasizer NanoZSP (Malvern, UK). FTIR spectra were recorded on a Thermo Fisher Scientific Nicolet iS50 FTIR spectrometer (Thermo Fisher Scientific, USA). XPS spectra were obtained on a Thermo Fisher Scientific Nexsa G2 X (Thermo Fisher Scientific, USA). High-resolution TEM images were recorded on a Tecnai G2 F30 (FEI, USA) transmission electron microscope at an acceleration voltage of 200 kV. The morphology of the nanozymes was observed by a SEM (Zeiss Ultra 55 microscope). The absorbance was recorded on a SpectraMax M2e microplate reader (Molecular Devices, USA). The cellular fluorescence images and histological staining images were recorded on a DMi8 fluorescence microscope (Leica, Germany). Quantitative analysis of ROS in cells and cellular uptake of nanozymes were measured on a flow cytometer (Beckman Coulter, cytoFLEX, USA). Fe, Zn, and Ca content in animal samples were tested by an ICP-OES (PerkinElmer, Avio 220 Max, USA). Ex vivo images were taken via an IVIS spectrum (PerkinElmer, USA). Electron paramagnetic resonance (EPR) spectra were recorded on a Bruker A300 spectrometer (X-band, Bruker, Germany).

Synthesis of SPB

SPB was synthesized according to a previously reported method (*28*). The synthetic procedure was as follows: A total of 0.75 g of PVP and 0.0275 g of $K_3[Fe(CN)_6]$ were dissolved in 10 ml of 75% ethanol solution containing 0.01 M HCl. The reaction precursor solution was placed in a water bath at 80°C. The reaction proceeded for 3 hours and subsequently cooled to room temperature. The resulting dark blue reaction mixture was washed with water. After freeze-drying for 24 hours, the SPB nanozyme was obtained.

Synthesis of ultrasmall Zn^{2+} doped PB

Doping of PB with Zn^{2+} was performed following a previously reported hydrothermal protocol with slight modifications (*29*, *40*, *41*). The synthetic procedure was as follows: Twenty milliliters of water containing 20 μl of $ZnCl_2$ (13.6 mg ml^{-1}) and 40 μl of $FeCl_3$ (32.4 mg ml^{-1}) was heated at 60°C (solution A). Simultaneously, 20 ml of water containing 0.5 mM citric acid and 0.02 mM $K_4[Fe(CN)_6]\cdot 3H_2O$ was also heated at 60°C (solution B). Solution B was then slowly added dropwise to solution A using an injection pump at 60°C, with magnetic stirring, and maintained for 10 min. The resulting dark blue reaction mixture was rapidly cooled to room temperature, centrifuged at 5000*g* for 1 hour, and washed three times with water. The samples were then freeze-dried for 24 hours.

Synthesis of imidazoyl carbamate (PBAP-CDI)

Imidazoyl carbamate (PBAP-CDI) was synthesized according to a previously reported method (*42*). PBAP (1.10 g, 4.7 mmol) was dissolved in dry CH_2Cl_2 (15 ml), and CDI (1.219 g, 7.5 mmol) was added dropwise. The reaction mixture was stirred at room temperature for 3 hours, under N_2 protection. The product was extracted with water (15 ml × 3 times). Then, it was washed with saturated brine to remove the organics, dried over $MgSO_4$, and concentrated under vacuum to yield PBAP-CDI as a white solid. PBAP-CDI was directly used in the next step. ^{1}H nuclear magnetic resonance (NMR; 400 MHz, $CDCl_3$): δ 1.34 (s, 12H), 5.42 (s, 2H), 7.06 (s, 1H), 7.43 (m, 3H), 7.85 (d, J = 8.0 Hz, 2H), 8.14 (s, 1H); ^{13}C NMR (100 MHz, $CDCl_3$): δ 24.8, 69.6, 83.9, 117.1, 127.7, 130.6, 135.2, 136.7, 137.1, and 148.4.

Synthesis of Oxi-DEX

Oxi-DEX was synthesized as follows (*31*). DEX (Mw = 10 kDa, 90 mg) was dissolved in 1.575 ml of anhydrous DMSO. To this solution, 149.3 mg of DMAP was added, followed by 364.6 mg of PBAP-CDI. The mixture was shaken overnight on a shaker plate under N_2 protection. The product was collected, and then it was precipitated in water and centrifuged at 10,250*g* for 15 min. The resulting pellet was washed with water three times and then freeze-dried for 24 hours.

Synthesis of ROS-responsive nanozyme (OZn)

ROS-responsive nanozyme (i.e., double emulsion particles containing SPBZn, termed SPBZn@Oxi-DEX or OZn) was synthesized by emulsion following a literature-reported method (*31*). First, Oxi-DEX (30.7 mg) was dissolved in 0.8 ml of $CHCl_3$ and 0.5 ml of methanol. Then, the SPBZn solution (4 mg/ml, 0.5 ml, in PBS) was added to the Oxi-DEX polymer solution and sonicated for 30 s on ice (with an output setting of 5 and a duty cycle of 80%). Next, a PVA solution [1.5 ml, 3% (w/w) in PBS] was added (0.5 ml each time), and the mixture was sonicated for 30 s on ice under the same settings. The resulting double emulsion was then poured into a second PVA solution [10 ml, 0.3% (w/w) in PBS] and stirred for 2 hours at room temperature. It was then centrifuged at 10,500*g* for 15 min and washed three times with water. The samples were freeze-dried for 36 hours.

Synthesis of FITC-OZn

First, FITC-labeled Oxi-DEX was synthesized (*42*). In detail, 1 g of Oxi-DEX was dissolved in 10 ml of dry DMSO. FITC (5 mg), dibutyltin

dilaurate (20 μl), and pyridine (40 μl) were added, and the mixture was stirred for 2 hours at 95°C under N_2 protection. Then, the mixture was centrifuged at 10,500*g* for 15 min and washed with water until the supernatant became colorless. The final solution was freeze-dried, and the FITC-labeled Oxi-DEX products were collected. Then, using the same procedure as the "Synthesis of ROS-responsive nanozyme (OZn)" section, FITC-OZn was synthesized.

Measurement of CAT-like activity

The CAT-like activity of the nanozymes was evaluated using the dopamine-enabled universal assay (*30*). Typically, a 200-μl reaction system in a 96-well plate containing 5-μl nanozyme, 90-μl tris buffer (10 mM, pH 8.5), 100-μl dopamine (2 mg/ml), and 5 μl H_2O_2 (0.8 M) was used. After the solution was added, the plate was quickly transferred to an anaerobic device. The plate was incubated at 37°C for 30 min, and the absorbance at 405 nm was measured using a microplate spectrophotometer.

Measurement of SOD-like activity

SOD-like activity was measured by detecting the elimination of $O_2^{\bullet-}$. According to the protocol for the SOD assay kits, 20 μl of nanozyme was mixed with 200 μl of WST-1 solution and 20 μl of enzyme solution in a 96-well plate. After incubation at 37°C for 20 min, the absorbance at 450 nm was measured using a microplate spectrophotometer.

Measurement of EPR

EPR spectra was used to measure the clearing activity of hydroxyl radicals (•OH). •OH was generated by the reaction of H_2O_2 and Fe^{2+}, which can be captured by DMPO. The reaction system contained H_2O_2 (0.5 mM), Fe^{2+} (5 μM), SPBZn nanozyme (20 or 50 μg/ml), and DMPO (22.5 mg/liter) in PBS buffer (pH 7.4). •OH generation was initiated by the addition of Fe^{2+}, followed by SPBZn, and EPR spectra were recorded immediately.

Cell culture

All types of cells were purchased from the Cell Bank of Type Culture Collection of Chinese Academy of Science (Shanghai, China). RAW-264.7 murine macrophages and A7R5 rat VSMCs were cultured in Dulbecco's modified Eagle's medium (DMEM) containing 10% fetal bovine serum (FBS), penicillin G sodium (100 U/ml), and streptomycin sulfate (100 μg/ml). A monocyte cell line (HL-60) and human umbilical vein endothelial cells (HUVECs) were cultured in RPMI 1640 medium containing 10% FBS, penicillin G sodium (100 U/ml), and streptomycin sulfate (100 μg/ml). All cells were cultured at 37°C in a humidified atmosphere containing 5% CO_2.

In vitro cytotoxicity evaluation

RAW264.7 cells, VSMCs, monocytes, and HUVECs were cultured in 96-well plates (1.0×10^4 cells per well) in 100 μl of DMEM or RPMI 1640 with 10% FBS, penicillin, and streptomycin for 12 hours. Cells were treated with various doses of PBZn and OZn. After 24-hour treatment, cell viability was measured using the CCK-8 assay.

Cellular uptake of OZn in vitro

RAW264.7 macrophages, monocytes, or VSMCs were seeded in a 12-well plate at a density of 3×10^5 cells per well. After incubation in 1 ml of growth medium for 12 hours, the cell culture medium was replaced with fresh medium containing FITC-labeled OZn (FITC-OZn) at various doses (10, 20, 50, and 100 μg/ml) and incubated for 4 hours. The cells were washed with PBS and collected, followed by quantification via flow cytometry. Fluorescence intensities were analyzed using FlowJo V.10.8.1 software.

Evaluation of intracellular ROS-scavenging ability

Intracellular ROS levels in RAW264.7 macrophages, monocytes, and VSMCs induced by H_2O_2 were evaluated using the fluorescent probe DCFH-DA. Cells were seeded in 12-well plates at a density of 1×10^5 per well and incubated in 1 ml of growth medium for 12 hours. The cell culture medium was then replaced with fresh medium containing different nanozymes and incubated for 2 hours, followed by stimulation with 100 μM H_2O_2 for 0.5 hours. The medium was removed, and 1 ml of fresh medium containing 10 μM DCFH-DA was added to each well. After incubating at 37°C for 30 min and washing three times with PBS, fluorescence microscopic imaging was performed. The intracellular ROS level was also monitored by flow cytometry.

Detection of calcification in VSMCs

Alizarin Red staining was used to assess the degree of cell calcification. VSMCs were seeded in a 12-well plate at a density of 8×10^4 cells per well and incubated in 1 ml of growth medium for 12 hours. Then, different nanozymes (50 μg ml^{-1}) were separately added and incubated with cells for 24 hours. Afterward, cells were incubated in a medium containing elevated Ca/Pi [2 mM $CaCl_2$ and 2.7 mM mixture of NaH_2PO_4 and Na_2HPO_4 (pH 7.4)] for 6 days. The cells were washed twice with PBS and fixed with 4% paraformaldehyde for 15 min. After washing with PBS, the cells were stained with 0.2% (w/v) Alizarin Red (pH 4.2) at room temperature for 30 min. Subsequently, the cells were thoroughly washed with water and observed by an optical microscopy. The Alizarin Red–stained area is proportional to the extent of calcium mineral deposition in the culture well.

In vitro apoptosis assay of VSMCs

Apoptosis analysis was performed using annexin V–FITC apoptosis detection kits with propidium iodide (PI), following the manufacturer's protocol. Specifically, VSMCs were seeded in a 12-well plate at 4×10^5 cells per well and incubated for 12 hours. The medium was then replaced with the fresh growth medium containing various nanozymes at a concentration of 25 μg ml^{-1}. After 12 hours of incubation, cells were treated with 100 μM H_2O_2 for 6 hours. The medium from each sample was collected, and the cells were washed three times with PBS, digested with 0.25 wt % trypsin, collected (by the medium collected before), and centrifuged. Then, the cells were resuspended in 195 μl of annexin V binding buffer with 5 μl of annexin V and 10 μl of PI viability staining solution at 1×10^5 cells ml^{-1}. Last, the cells were incubated in the dark for 20 min and monitored by flow cytometry.

Animals

All animal experiments were approved by the Institutional Animal Care and Use Committee (IACUC) of Nanjing University (IACUC-2306004). Male Sprague-Dawley rats (150 to 160 g) were supplied by Beijing Vital River Laboratory Animal Technology Co. Ltd. (China). All the animals were acclimatized to the laboratory for 7 days before experiments.

Establishment of AAA model in rats

Elastin damage in the abdominal aortic of rats was induced using the perivascular application of anhydrous calcium chloride ($CaCl_2$), based on previously established protocols (*43*, *44*). Briefly, following anesthesia, the infrarenal abdominal aorta was exposed, and a sterile cotton gauze (0.5 cm by 0.5 cm) soaked in $CaCl_2$ solution (0.50 M) was applied to the aorta for 15 min. The treated area was then rinsed with saline, and the abdominal incision was closed with sutures. Iodine-soaked cotton balls were used to sterilize the incision. Rats in the normal control (AAA^-) group underwent the same surgical procedure but were treated with saline instead of $CaCl_2$.

In vivo targeting capability of OZn nanozymes

First, the AAA model in rats was established by $CaCl_2$. Then, FITC-labeled OZn was injected in randomly assigned AAA^+ rats via the tail vein on day 14 postsurgery. Rats in the model group (AAA^+ rats) also received an intravenous injection of saline, while those in the sham group (AAA^- rats) received an intravenous injection of FITC-labeled OZn. Each rat was housed in standard rat cages alone, and the urine was collected. After 8 hours, the animals were euthanized. The entire aortas, including the thoracic aorta, abdominal aorta, and bilateral iliac arteries, were harvested. Major organs, including the heart, liver, spleen, lungs, and kidneys, were also collected. After washing with PBS, the samples were imaged using an IVIS instrument. Fluorescence intensities were quantified using Living Image 4.5 software.

Study on retention time of OZn at the lesion site

In a separate experiment (Fig. 4F), the retention of OZn at the aneurysm site was observed after tail vein injection. On day 14 post–AAA model establishment, FITC-labeled OZn was injected via the tail vein, and urine samples were collected. Rats were euthanized at 3, 12, and 24 hours postinjection (three rats per time point). The entire aorta and major organs were harvested and observed using an IVIS instrument.

Therapeutic efficacy of different nanozymes on rats with $CaCl_2$-induced AAA

To evaluate the therapeutic efficacy of different nanozymes on rats with AAA, rats were randomly assigned into five groups ($n = 5$) (Fig. 6A). On day 2 postinjury, rats in the model group were intravenously injected with saline, while rats in other groups received different nanozymes (5 mg/kg) twice a week for 3 weeks. The sham group (AAA^- rats) received saline injections. On day 23, the rats were euthanized, and the abdominal aortas with induced aneurysms were exposed and harvested. Midsections of the abdominal aortas were prepared as paraffin sections (5 μm) and stained with Alizarin Red, H&E, and EVG. Sections were also stained with anti–MMP-9 antibody (catalog no. GB15132-100, Servicebio, China), anti–MMP-2 antibody (catalog no. GB111507-100, Servicebio, China), anti–α-SMA antibody (catalog no. ET1607-53, HUABIO, China), and anti-CDF4/80 antibody (catalog no. GB113373-100, Servicebio, China). In addition, the abdominal aorta was frozen directly in optimal cutting temperature (O.C.T) Compound and sectioned at a thickness of 8 μm. The obtained cryosections were incubated with DHE (10 μM) for 30 min. After washing with PBS three times, the cryosections were imaged with a fluorescence microscope. Calcium contents in the abdominal aortas were weighted and dissolved in nitric acid for ICP-OES measurement.

Therapeutic efficacy of OZn on aneurysms induced by long-term $CaCl_2$ injury

A total of 25 rats were used and divided into five groups. The normal group underwent sham surgery. After the AAA model was established, the remaining 20 rats were randomly divided into four groups (five rats per group): model, SPBZn, OZn, and clopidogrel. Treatments were commenced on day 10 postsurgery. The normal and model groups received saline injections, while the remaining groups received SPBZn, OZn, and clopidogrel injections (5 mg/kg). Treatments were administered every 3 days for a total of four treatments. On day 26, the experiment was concluded, and rats were euthanized for analysis.

Correlation between urinalysis and disease progression

We evaluated the correlation between urinalysis and disease progression in another separate experiment (Fig. 7J). On the 10th day after establishing the $CaCl_2$-induced AAA model, treatments were begun, with nanozymes administered every 2 days. Two treatments constituted one treatment stage. The experiment was divided into three stages, with four rats in each stage. Urine samples were collected on the day following the completion of each treatment stage, and the rats were euthanized. Urine was also collected on the 9th and 11th days to assess the changes in CAT-like activity in the urine before and after OZn injection.

Statistical analysis

All data are presented as the means ± SD. One-way analysis of variance (ANOVA) and Student's *t* test were used for statistical analyses. Values of $^*P < 0.05$, $^{**}P < 0.01$, $^{***}P < 0.001$, and $^{****}P < 0.0001$ were applied to annotate statistical significance. The data of ICP-OES analysis of the content of Fe and Zn in the urine and statistical analysis to compare median values between groups were determined by the Mann-Whitney *U* test.

AI-assisted language polishing

AI tools, including ChatGPT (GPT-5) and DeepSeek (version 2.0), were used solely for linguistic refinement, specifically for grammar correction, optimization of sentence structure, and improvement of expression fluency. The authors declare that these tools were not involved in experimental design, data analysis, or formulation of scientific conclusion. Prompt used: "Please check and polish the following text for grammar errors and improve its academic readability while retaining the original scientific meaning."

Supplementary Materials

This PDF file includes:

Figs. S1 to S32
Table S1

REFERENCES AND NOTES

1. N. Sakalihasani, J.-B. Michel, A. Katsargyris, H. Kuivaniemi, J.-O. Defraigne, A. Nchimi, J. T. Powell, K. Yoshimura, R. Hultgren, Abdominal aortic aneurysms. *Nat. Rev. Dis. Primers* **4**, 34 (2018).
2. J. Gao, H. Cao, G. Hu, Y. Wu, Y. Xu, H. Cui, H. Lu, L. Zheng, The mechanism and therapy of aortic aneurysms. *Signal Transduct. Target. Ther.* **8**, 55 (2023).
3. E. L. Chaikof, R. L. Dalman, M. K. Eskandari, B. M. Jackson, W. A. Lee, M. A. Mansour, T. M. Mastracci, M. Mell, M. H. Murad, L. L. Nguyen, G. S. Oderich, M. S. Patel, M. L. Schermerhorn, B. W. Starnes, The Society for Vascular Surgery practice guidelines on the care of patients with an abdominal aortic aneurysm. *J. Vasc. Surg.* **67**, 2–77.e2 (2018).
4. A. Wanhainen, I. Van Herzeele, F. B. Goncalves, S. B. Montoya, X. Berard, J. R. Boyle, M. D'Oria, C. F. Prendes, C. D. Karkos, A. Kazimierczak, M. J. W. Koelemay, T. Kölbel, K. Mani, G. Melissano, J. T. Powell, S. Trimarchi, N. Tsilimparis, ESVS Guidelines Committee, G. A. Antoniou, M. Björck, R. Coscas, N. V. Dias, P. Kolh, S. Lepidi, B. M. E. Mees, T. A. Resch,

J. B. Ricco, R. Tulamo, C. P. Twine, D. Reviewers, D. Branzan, S. W. K. Cheng, R. L. Dalman, F. Dick, J. Golledge, S. Haulon, J. A. van Herwaarden, N. S. Ilic, A. Jawien, T. M. Mastracci, G. S. Oderich, F. Verzini, K. K. Yeung, European Society for Vascular Surgery (ESVS) 2024 clinical practice guidelines on the management of abdominal aorto-iliac artery aneurysms. *Eur. J. Vasc. Endovasc. Surg.* **67**, 192–331 (2024).
5. K. C. Kent, Abdominal aortic aneurysms. *N. Engl. J. Med.* **371**, 2101–2108 (2014).
6. P. K. Gupta, B. Ramanan, T. L. Engelbert, G. Tefera, J. R. Hoch, K. C. Kent, A comparison of open surgery versus endovascular repair of unstable ruptured abdominal aortic aneurysms. *J. Vasc. Surg.* **60**, 1439–1445 (2014).
7. J. Golledge, Abdominal aortic aneurysm: Update on pathogenesis and medical treatments. *Nat. Rev. Cardiol.* **16**, 225–242 (2019).
8. N. L. Weintraub, Understanding abdominal aortic aneurysm. *N. Engl. J. Med.* **361**, 1114–1116 (2009).
9. S. E. Hensley, G. R. Upchurch Jr., Repair of abdominal aortic aneurysms. *J. Am. Coll. Cardiol.* **80**, 821–831 (2022).
10. A. Klink, F. Hyafil, J. Rudd, P. Faries, V. Fuster, Z. Mallat, O. Meilhac, W. J. M. Mulder, J. B. Michel, F. Ramirez, G. Storm, R. Thompson, I. C. Turnbull, J. Egido, J. L. Martín-Ventura, C. Zaragoza, D. Letourneur, Z. A. Fayad, Diagnostic and therapeutic strategies for small abdominal aortic aneurysms. *Nat. Rev. Cardiol.* **8**, 338–347 (2011).
11. J. Raffort, F. Lareyre, M. Clément, R. Hassen-Khodja, G. Chinetti, Z. Mallat, Monocytes and macrophages in abdominal aortic aneurysm. *Nat. Rev. Cardiol.* **14**, 457–471 (2017).
12. J.-B. Michel, J.-L. Martin-Ventura, J. Egido, N. Sakalihasan, V. Treska, J. Lindholt, E. Allaire, U. Thorsteinsdottir, G. Cockerill, J. Swedenborg, FAD EU Consortium, Novel aspects of the pathogenesis of aneurysms of the abdominal aorta in humans. *Cardiovasc. Res.* **90**, 18–27 (2011).
13. M. L. McCormick, D. Gavrila, N. L. Weintraub, Role of oxidative stress in the pathogenesis of abdominal aortic aneurysms. *Arterioscler. Thromb. Vasc. Biol.* **27**, 461–469 (2007).
14. F. J. Miller Jr., W. J. Sharp, X. Fang, L. W. Oberley, T. D. Oberley, N. L. Weintraub, Oxidative stress in human abdominal aortic aneurysms: A potential mediator of aneurysmal remodeling. *Arterioscler. Thromb. Vasc. Biol.* **22**, 560–565 (2002).
15. A. L. Durham, M. Y. Speer, M. Scatena, C. M. Giachelli, C. M. Shanahan, Role of smooth muscle cells in vascular calcification: Implications in atherosclerosis and arterial stiffness. *Cardiovasc. Res.* **114**, 590–600 (2018).
16. P. Petsophonsakul, M. Furmanik, R. Forsythe, M. Dweck, G. W. Schurink, E. Natour, C. Reutelingsperger, M. Jacobs, B. Mees, L. Schurgers, Role of vascular smooth muscle cell phenotypic switching and calcification in aortic aneurysm formation involvement of vitamin k-dependent processes. *Arterioscler. Thromb. Vasc. Biol.* **39**, 1351–1368 (2019).
17. J. Golledge, J. Muller, A. Daugherty, P. Norman, Abdominal aortic aneurysm: Pathogenesis and implications for management. *Arterioscler. Thromb. Vasc. Biol.* **26**, 2605–2613 (2006).
18. R. A. Quintana, W. R. Taylor, Cellular mechanisms of aortic aneurysm formation. *Circ. Res.* **124**, 607–618 (2019).
19. I. Parastatidis, D. Weiss, G. Joseph, W. R. Taylor, Overexpression of catalase in vascular smooth muscle cells prevents the formation of abdominal aortic aneurysms. *Arterioscler. Thromb. Vasc. Biol.* **33**, 2389–2396 (2013).
20. P. Ramos-Mozo, J. Madrigal-Matute, R. Martinez-Pinna, L. M. Blanco-Colio, J. A. Lopez, E. Camafeita, O. Meilhac, J. B. Michel, C. Aparicio, M. V. de Ceniga, J. Egido, J. L. Martín-Ventura, Proteomic analysis of polymorphonuclear neutrophils identifies catalase as a novel biomarker of abdominal aortic aneurysm: Potential implication of oxidative stress in abdominal aortic aneurysm progression. *Arterioscler. Thromb. Vasc. Biol.* **31**, 3011–3019 (2011).
21. W. Zhang, S. Hu, J.-J. Yin, W. He, W. Lu, M. Ma, N. Gu, Y. Zhang, Prussian blue nanoparticles as multienzyme mimetics and reactive oxygen species scavengers. *J. Am. Chem. Soc.* **138**, 5860–5865 (2016).
22. X. Meng, H. Fan, L. Chen, J. He, C. Hong, J. Xie, Y. Hou, K. Wang, X. Gao, L. Gao, X. Yan, K. Fan, Ultrasmall metal alloy nanozymes mimicking neutrophil enzymatic cascades for tumor catalytic therapy. *Nat. Commun.* **15**, 1626 (2024).
23. C. N. Loynachan, A. P. Soleimany, J. S. Dudani, Y. Lin, A. Najer, A. Bekdemir, Q. Chen, S. N. Bhatia, M. M. Stevens, Renal clearable catalytic gold nanoclusters for in vivo disease monitoring. *Nat. Nanotechnol.* **14**, 883–890 (2019).
24. Y. Zhang, G. Wei, W. Liu, T. Li, Y. Wang, M. Zhou, Y. Liu, X. Wang, H. Wei, Nanozymes for nanohealthcare. *Nat. Rev. Methods Primers* **4**, 36 (2024).
25. R. Zhang, B. Jiang, K. Fan, L. Gao, X. Yan, Designing nanozymes for in vivo applications. *Nat. Rev. Bioeng.* **2**, 849–868 (2024).
26. S. Ji, B. Jiang, H. Hao, Y. Chen, J. Dong, Y. Mao, Z. Zhang, R. Gao, W. Chen, R. Zhang, Q. Liang, H. Li, S. Liu, Y. Wang, Q. Zhang, L. Gu, D. Duan, M. Liang, D. Wang, X. Yan, Y. Li, Matching the kinetics of natural enzymes with a single-atom iron nanozyme. *Nat. Catal.* **4**, 407–417 (2021).
27. C. Huang, C. Zhao, Q. Deng, H. Zhang, J. Ren, D. Yu, X. Qu, Hydrogen-bonded organic framework-based bioorthogonal catalysis prevents drug metabolic inactivation. *Nat. Catal.* **6**, 729–739 (2023).
28. Z. Qin, B. Chen, Y. Mao, C. Shi, Y. Li, X. Huang, F. Yang, N. Gu, Achieving ultrasmall Prussian blue nanoparticles as high-performance biomedical agents with multifunctions. *ACS Appl. Mater. Interfaces* **12**, 57382–57390 (2020).
29. P. Shou, Z. Yu, Y. Wu, Q. Feng, B. Zhou, J. Xing, C. Liu, J. Tu, O. U. Akakuru, Z. Ye, X. Zhang, Z. Lu, L. Zhang, A. Wu, Zn^{2+} doped ultrasmall Prussian blue nanotheranostic agent for breast cancer photothermal therapy under mr imaging guidance. *Adv. Healthc. Mater.* **9**, e1900948 (2020).
30. A. Lin, Q. Liu, Y. Zhang, Q. Wang, S. Li, B. Zhu, L. Miao, Y. Du, S. Zhao, H. Wei, A dopamine-enabled universal assay for catalase and catalase-like nanozymes. *Anal. Chem.* **94**, 10636–10642 (2022).
31. K. E. Broaders, S. Grandhe, J. M. J. Fréchet, A biocompatible oxidation-triggered carrier polymer with potential in therapeutics. *J. Am. Chem. Soc.* **133**, 756–758 (2011).
32. Q. Zhang, H. Tao, Y. Lin, Y. Hu, H. An, D. Zhang, S. Feng, H. Hu, R. Wang, X. Li, J. Zhang, A superoxide dismutase/catalase mimetic nanomedicine for targeted therapy of inflammatory bowel disease. *Biomaterials* **105**, 206–221 (2016).
33. S. Jono, M. D. McKee, C. E. Murry, A. Shioi, Y. Nishizawa, K. Mori, H. Morii, C. M. Giachelli, Phosphate regulation of vascular smooth muscle cell calcification. *Circ. Res.* **87**, e10–e17 (2000).
34. C. M. Shanahan, M. H. Crouthamel, A. Kapustin, C. M. Giachelli, Arterial calcification in chronic kidney disease: Key roles for calcium and phosphate. *Circ. Res.* **109**, 697–711 (2011).
35. C. C. Hsieh, M. H. Yen, C. H. Yen, Y. T. Lau, Oxidized low density lipoprotein induces apoptosis via generation of reactive oxygen species in vascular smooth muscle cells. *Cardiovasc. Res.* **49**, 135–145 (2001).
36. D. I. Brown, K. K. Griendling, Regulation of signal transduction by reactive oxygen species in the cardiovascular system. *Circ. Res.* **116**, 531–549 (2015).
37. D. Yamanouchi, S. Morgan, C. Stair, S. Seedial, J. Lengfeld, K. C. Kent, B. Liu, Accelerated aneurysmal dilation associated with apoptosis and inflammation in a newly developed calcium phosphate rodent abdominal aortic aneurysm model. *J. Vasc. Surg.* **56**, 455–461 (2012).
38. S. Pustylnikov, D. Sagar, P. Jain, Z. K. Khan, Targeting the C-type lectins-mediated host-pathogen interactions with dextran. *J. Pharm. Pharm. Sci.* **17**, 371–392 (2014).
39. U. Klotz, H. Kroemer, Clinical pharmacokinetic considerations in the use of plasma expanders. *Clin. Pharmacokinet.* **12**, 123–135 (1987).
40. X. Cai, W. Gao, L. Zhang, M. Ma, T. Liu, W. Du, Y. Zheng, H. Chen, J. Shi, Enabling Prussian blue with tunable localized surface plasmon resonances: Simultaneously enhanced dual-mode imaging and tumor photothermal therapy. *ACS Nano* **10**, 11115–11126 (2016).
41. W. Zhu, K. Liu, X. Sun, X. Wang, Y. Li, L. Cheng, Z. Liu, Mn^{2+}-doped Prussian blue nanocubes for bimodal imaging and photothermal therapy with enhanced performance. *ACS Appl. Mater. Interfaces* **7**, 11575–11582 (2015).
42. H. Wang, W.-G. Li, K. Zeng, Y.-J. Wu, Y. Zhang, T.-L. Xu, Y. Chen, Photocatalysis enables visible-light uncaging of bioactive molecules in live cells. *Angew. Chem. Int. Ed. Engl.* **58**, 561–565 (2019).
43. W. Lin, K. Hu, C. Li, W. Pu, X. Yan, H. Chen, H. Hu, H. Deng, J. Zhang, A multi-bioactive nanomicelle-based "One Stone for Multiple Birds" strategy for precision therapy of abdominal aortic aneurysms. *Adv. Mater.* **34**, 2204455 (2022).
44. J. Cheng, R. Zhang, C. Li, H. Tao, Y. Dou, Y. Wang, H. Hu, J. Zhang, A targeting nanotherapy for abdominal aortic aneurysms. *J. Am. Coll. Cardiol.* **72**, 2591–2605 (2018).

Acknowledgments

Funding: This work was supported by the National Natural Science Foundation of China (22374071 to H.W.), the Key Program of Nanozyme Laboratory in Zhongyuan (NLZ-KP2024NIC06 to H.W.), the Jiangsu Provincial Key R&D Program (BE2022836 to H.W.), the State Key Laboratory of Analytical Chemistry for Life Science (5431ZZXM2501 and 5431ZZXM2306 to H.W.), the National Key R&D Program of China (2021YFF1200700 and 2019YFA0709200 to H.W.), the Fundamental Research Funds for the Central Universities (2025300292 to H.W.), and the Open Funds of NMPA Key Laboratory for Biomedical Optics (20240001 to H.W.). We are thankful for the kind help from the Yachen Foundation of Nanjing University, PAPD Program and the International Expansion and Enhancement Program by Nanjing University International Affairs Office. **Author contributions:** Writing—original draft: H.W., W.L., and Y. Z. Conceptualization: H.W., W.L., Y. Z., X.C., and Q.S. Investigation: H.W., W.L., Y.Z., X.C., Q.S., and S.H. Writing—review and editing: H.W., W.L., Y.Z., X.C., Q.S., X.G., T.L., S.H., and Z.Q. Methodology: H.W., W.L., Y.Z., X.C., and Q.S. Resources: H.W., W.L., Y.Z., X.C., Q.S., S.H., and Z.Q. Funding acquisition: H.W. Data curation: H.W., W.L., Y.Z., X.C., and Q.S. Validation: H.W., W.L., Y.Z., X.C., Q.S., and X.G. Supervision: H.W., W.L., Y.Z., X.C., and Q.S. Formal analysis: H.W., W.L., Y.Z., X.C., and Q.S. Software: H.W., W.L., Y.Z., X.C., and Q.S. Software: H.W., W.L., X.C., and Q.S. Project administration: H.W., W.L., Y.Z., X.C.,

and Q.S. Visualization: H.W., W.L., Y. Z., X.C., and Q.S. **Competing interests:** The authors declare that they have no competing interests. **Data and materials availability:** All data needed to evaluate the conclusions in the paper are present in the paper and/or the Supplementary Materials.

Submitted 28 May 2025
Accepted 5 November 2025
Published 3 December 2025
10.1126/sciadv.adz3713